JACS
JOURNAL OF THE AMERICAN CHEMICAL SOCIETY
Article
pubs.acs.org/JACS

SnS_4^{4-}, SbS_4^{3-}, and AsS_3^{3-} Metal Chalcogenide Surface Ligands: Couplings to Quantum Dots, Electron Transfers, and All-Inorganic Multilayered Quantum Dot Sensitized Solar Cells

Ho Jin,[†,#] Sukyung Choi,[†,#] Guichuan Xing,[‡,§,∥] Jung-Hoon Lee,[⊥] Yongju Kwon,[†] Wee Kiang Chong,[‡] Tze Chien Sum,[‡,§,∥] Hyun Myung Jang,[⊥] and Sungjee Kim*[,†]

[†]Department of Chemistry, Pohang University of Science and Technology, Pohang 790-784, South Korea
[‡]Division of Physics and Applied Physics, School of Physical and Mathematical Sciences, Nanyang Technological University, 21 Nanyang Link, Singapore 637371
[§]Energy Research Institute @NTU (ERI@N), Research Techno Plaza, X-Frontier Block, Level 5, 50 Nanyang Drive, Singapore 637553,
[∥]Singapore−Berkeley Research Initiative for Sustainable Energy, 1 Create Way, Singapore 138602
[⊥]Department of Material Science and Engineering and Division of Advanced Materials Science, Pohang University of Science and Technology, Pohang 790-784, South Korea

Supporting Information

ABSTRACT: Three inorganic capping ligands (ICLs) for quantum dots (QDs), SnS_4^{4-}, SbS_4^{3-} and AsS_3^{3-}, were synthesized and the energy levels determined. Proximity between the ICL LUMO and QD conduction level governed the electronic couplings such as absorption shift upon ligand exchange, and electron transfer rate to TiO_2. QD-sensitized solar cells were fabricated, using the ICL-QDs and also using QD multilayers layer-by-layer assembled by bridging coordinations, and studied as a function of the ICL ligand and the number of QD layers.

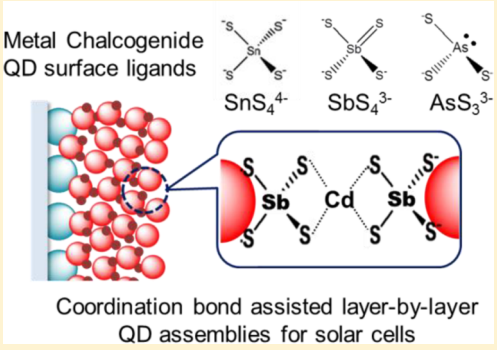

INTRODUCTION

Semiconductor nanocrystal quantum dots (QDs) have received great interest as an alternative for conventional organic sensitizers for photovoltaic (PV) applications because of the high extinction coefficients, broad absorptions, band gap tunability, robustness against photobleaching, and their capability in constructing sophisticated structures such as multilayered or hybrid sensitizers.[1,2] For efficient QD-sensitized solar cells (QDSCs), successful extractions of photogenerated carriers need to be guaranteed from QDs to external electrodes through a series of charge separations and transport processes. Typically, the QDSC has a donor-bridge-acceptor structure that consists of bifunctional molecules between mesoporous oxide films and QDs. The bridge molecule plays a pivotal role in the QDSC efficiency, and variations of the bridge molecules (i.e., length, conjugation, and surface anchoring functional group) strongly affect the carrier transport and photovoltaic properties of the QDSCs.[3−6] Recently, Talapin and co-workers reported molecular metal chalcogenide complexes serving as inorganic capping ligands (ICLs) for QDs.[7,8] When close-packed and annealed by heat, QDs with ICLs showed band-like transport with high electron mobility and high photoconductivity, thereby demonstrating the enhanced electronic couplings between QDs.[9] Such transport phenomena in QD solids were very dependent on the ICL; arrays of CdSe QDs capped with $In_2Se_4^{2-}$ showed the electron mobility as high as 16 $cm^2\ V^{-1}\ s^{-1}$,[9] whereas those capped with $Sn_2S_6^{4-}$ exhibited 3×10^{-2} $cm^2\ V^{-1}\ s^{-1}$.[7] ICLs are relatively small and can be an ideal QDSC bridge molecule that links neighboring QDs in close proximity. However, ICL-QDs have shown only limited success in photovoltaic applications so far. For example, Korgel and co-workers studied $CuInSe_2$ QD solar cells using ICLs, where they reported power conversion efficiency (PCE) that is only comparable to oleylamine-capped QDSCs.[10] We have previously compared the effect of SnS_4^{4-} ligand, S^{2-} metal free ligand, and organic surface ligands for QDSCs, where ICL-QDs failed to show noticeably enhanced photovoltaic properties.[11] Interestingly, the dominating effect of the ICL was affected by its position; i.e., whether (i) the ICLs were located in between the QD and photoanode or (ii) the ICLs were facing outside and were mostly interacting with electrolytes.

Received: June 4, 2015
Published: October 13, 2015

DOI: 10.1021/jacs.5b05787
J. Am. Chem. Soc. 2015, 137, 13827−13835

For example, S^{2-} ligands trap holes. When exposed to electrolytes, these ligands expedite hole transfers and thus enhance the PV performance. However, when bridged in between the QD and photoanode, the trapped holes mostly annihilate with the photoelectrons from QDs. Therefore, ICLs should be compared, and their characteristics understood before they can be properly exploited for QD PV applications.

In this report, we compare three ICLs (SnS_4^{4-}, SbS_4^{3-} and AsS_3^{3-}, Figure 1a) for QDSCs. This is also the first report, to

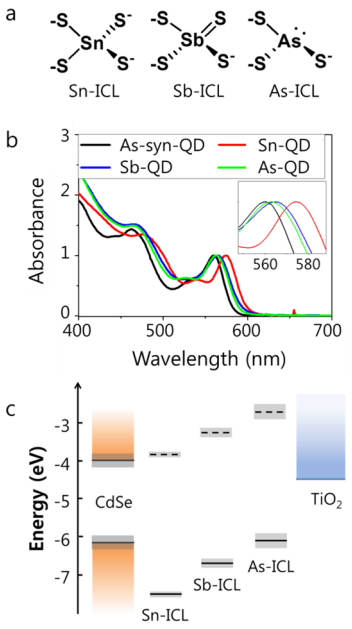

Figure 1. (a) Molecular structures of Sn-ICL, Sb-ICL, and As-ICL. (b) Absorption spectra of CdSe QD samples with different surface ligand molecules: as-synthesized QD (As-syn-QD), Sn-ICL surfaced QD (Sn-QD), Sb-ICL surfaced QD (Sb-QD) and As-ICL surfaced QD (As-QD). The inset shows enlarged portion of the spectra around the first excitonic peaks. (c) Energy diagrams for the conduction and valence levels of 3.6 nm sized CdSe QD (orange), the HOMO and LUMO levels of Sn-ICL, Sb-ICL, and As-ICL molecules (black), and the conduction level of TiO_2 (blue). The gray shades represent the standard deviations.

the best of authors' knowledge, using SbS_4^{3-} as ICL of QDs. One of major advantages of using QDs for PV applications is that QDs can be assembled into sophisticated nanostructures such as layer-by-layer (LbL) assembled QD multilayers. Multilayered QDSCs can efficiently absorb photons and funnel the energies through the QD layers which show cascading band level alignments.[12,13] We have previously reported LbL QD multilayer PV devices, where the LbL assembly was achieved by exploiting electrostatic interactions between QD surfaces.[14,15] In this report, we LbL assembled QD multilayers by exploiting metal−ligand coordinations between ICLs on QDs and bridging metal ions. This strategy can be useful for efficient and all-inorganic PV devices that incorporate "conductive" QD arrays.

RESULTS AND DISCUSSION

SnS_4^{4-} and AsS_3^{3-} ICLs were prepared by following the hydrazine-free procedures reported by Talapin and co-workers.[8] SbS_4^{3-} was obtained by reacting $Na_3SbS_4{\cdot}9H_2O$ with Na_2S in aqueous solution (Experimental Section). The synthesized ICLs were characterized by EDX, NMR, and mass spectroscopy (Figure S1). Figure 1a shows the molecular structures of the three ICLs. 3.6 nm CdSe QDs were prepared by following a protocol reported previously (Experimental Section). The QDs were ligand-exchanged by ICLs by one-phase method (Experimental Section). ICL-exchanged QDs were dispersed in water, and excess ICLs were removed by dialysis. Complete ligand exchange by ICLs was confirmed by the removal of organic vibrations such as C−H stretchings in FTIR (Figure S2a). Their particle size distribution as determined by dynamic light scattering was ∼5 nm, which means that the aqueous solution is free of aggregation (Figure S2b). The QDs ligand-exchanged by SnS_4^{4-}, SbS_4^{3-}, and AsS_3^{3-} ICLs (noted as Sn-QD, Sb-QD, and As-QD, respectively) showed slightly different absorption profiles (Figure 1b). Sn-QD showed the largest red shift of the excitonic peak (54 meV), which was followed by Sb-QD (19 meV) and As-QD (10 meV). The red shifts are indicative of strong couplings between QD and the ICL and the resultant new and less-confining states by the QD-ICL interface.[16,17] The degree of mixing between QD levels and ICL states depends mainly on two factors: (i) overlap V between the orbitals and (ii) the energy gap $\Delta\varepsilon$ between the QD and ICL states. Each pairwise coupling between QD level and ICL state split from the original states by energy approximately proportional to $V^2/\Delta\varepsilon$.[17]

The three SnS_4^{4-}, SbS_4^{3-}, and AsS_3^{3-} ICLs (noted as Sn-ICL, Sb-ICL, and As-ICL, respectively) are similar in size and geometry (Figure 1a). Sn-ICL has the tetrahedral shape with the Sn−S length of 2.4 Å and the S−Sn−S angle ∼110°.[18] Sb-ICL is also tetrahedral with the Sb−S length of 2.3 Å and the S−Sb−S angle ∼109°.[19] As-ICL forms a trigonal pyramidal geometry with the As−S length of 2.3 Å and the S−As−S angle of 102°.[20] All three ICLs are hypothesized to share a similar binding mode onto QD surfaces, acting like a bidentate ligand using two thiolates (M−S^-, M: central metal atom) chelating Cd atoms on QD surfaces. The three ICLs may bind onto QD surfaces by monodentate, bidentate, or tridentate fashion. Considering many bidentate QD anchoring moieties such as carboxylate, phosphonate, and dithiocarbamate which share similar geometries as the ICLs, it is unlikely for the ICLs to act as monodentate ligands.[21−23] Tridentate binding fashion of the ICLs to QD surface may be too bulky and not optimal considering the neighboring selenium surface atoms. Recent EXAFS studies also suggest dominant bidentate binding of SnS_4^{4-} onto QD surface.[24] In the case of As-QD, tridentate binding of the As-ICL cannot provide the QD colloidal stability because it allows no extra available charge for the bound As-ICLs. To the contrary, well-dispersed As-QD samples were always observed with the moderately high zeta potential value. The zeta potentials were measured for Sn-QD, Sb-QD, and As-QD (−46, −22, and −18 mV, respectively, Figure S2c). Upon QD surface binding, Sn-ICL, Sb-ICL, and As-ICL have two thiolates, one dithiocarboxylate, and one thiolate respectively, remaining available to the outside, if the ICLs acted as bidentate ligands. For the case, the available number of surface charges per ICL is two for Sn-ICL, one for Sb-ICL, and one for As-ICL, which coincides well with the QD zeta potential measurements. We assume an identical ICL surface density on QD for the three ICL-QDs. The initial organic ligand was oleic acid, which is known to bind Cd atoms on QD surface. As confirmed by the FTIR measurements, the initial ligands on QDs were completely replaced by the ICL ligands which are supposed to compete the same binding sites of Cd atoms on QD surface. The complete replacement of initial ligands with

DOI: 10.1021/jacs.5b05787
J. Am. Chem. Soc. 2015, 137, 13827−13835

supposedly no additional ICL surface binding sites other than the sites preoccupied by oleic acids makes the hypothesis of identical ICL surface density quite reasonable. It is also noted that the zeta potential ratio of 2:1:1 for the Sn-QD, Sb-QD, and As-QD was reproducibly observed.

In order to understand the symmetry of frontier orbitals of the three ICLs, we performed density functional theory (DFT) calculations on the ICLs to estimate the spatial electron distributions of the orbitals (Figure S3a).

H-passivation was adopted for all the ICLs to mimic the effect of charged state of the sulfur atoms. The HOMO of Sn-ICL is characterized by T_d symmetry while those of Sb- and As-ICL are characterized by C_{3v} symmetry. The HOMOs of Sn- and Sb-ICL are composed of nonbonding S 3*p* orbitals. In the case of As-ICL, interestingly, the HOMO of As-ICL is composed of the molecular orbital between As 4*s* − 4*p* self-mixed orbital and S 3*p* orbital. Due to this, the HOMO of As-ICL shows asymmetric electron density near As atom, which is typical for lone pair formation. The LUMOs of Sn- and Sb-ICL are characterized by T_d symmetry while that of As-ICL is characterized by Cs symmetry that has only a mirror plane. The LUMOs of Sn- and Sb-ICL are commonly composed of Sn (and Sb) 5*s* − S 3*p* antibonding state. Thus, the symmetry of the two LUMOs are very alike to each other. The LUMO of As-ICL is composed of As (4*s* − 4*p*) − S 3*p* antibonding state. In this case, As 4*s* − 4*p* self-mixed orbital is forming a hybridization orbital with two adjacent S 3*p* orbitals which show the same orbital phase. Symmetry of HOMOs is invariant for the Sb- and As-ICLs, and symmetry of LUMOs is invariant for the Sn- and Sb-ICL. Considering the structural distortion of ICLs upon the binding on QD surface, all three ICLs may also share a similar symmetry. Since the three ICLs can be thought to bind similarly onto QD surfaces by the dithiolate binding fashion and share the similar bond length and geometry, the overlap *V* between the QD and ICL states should be not much different for the three ICLs. As a result, the degree of mixing should be considered to be strongly related to the energy gaps (or energy levels of ICLs). For an example, Sn- and Sb-ICLs share the same T_d symmetry for the LUMOs but Sn- and Sb-QDs show the large difference in the degree of red shift for the excitonic peaks (54 meV vs 19 meV).

The energy levels of the three ICLs with respect to our QD were obtained (Figure 1c). Ultraviolet photoelectron spectroscopy (UPS) was performed to determine the HOMO levels of ICLs (−7.43 eV for Sn-ICL, −6.58 eV for Sb-ICL and −6.12 eV for As-ICL. Figure S4 for the UPS data and Table S1 for the detailed method). The ICL LUMO levels (−3.79 eV for Sn-ICL, −3.23 eV for Sb-ICL and −2.74 eV for As-ICL) were estimated by the optical band gaps (Figure S 4d−f and Table S2). The HOMO LUMO gaps obtained by the optical energy gaps (3.64 eV for Sn-ICL, 3.35 eV for Sb-ICL and 3.38 eV for As-ICL) were compared with calculated values by simulations using density functional theory (3.67 eV for Sn-ICL, 3.42 eV for Sb-ICL and 3.37 eV for As-ICL), which showed fairly good agreements (Figure S3b). The valence level (−6.21 eV) of the CdSe QD was also determined by UPS (Figure S5). The conduction level (−4.00 eV) of quantum confined CdSe QD was estimated from the optical band gap (2.21 eV). The conduction level of CdSe QD for 3.6 nm diameter agreed well with the previously reported value.[25] The energy gaps between the QD conduction level and the LUMO of Sn-ICL, Sb-ICL, and As-ICL are 0.21, 0.77, 1.26 eV, respectively. The gaps between the QD valence level and the three ICL HOMOs are 1.22, 0.37, 0.09 eV, respectively. Considering the largest red-shift observed for Sn-QD after the ligand-exchange, the conduction QD level couples more strongly with ICL LUMO than does the QD valence with HOMO. The difference may be a result of the characteristics of our ICLs and also of the lighter effective mass of electrons than holes allowing the wave function spreading further out to the surface. The energy gap ($\Delta\varepsilon$) was inversely proportional to the absorption shift (Figure S6). As $\Delta\varepsilon$ decreases, the strength of the electronic coupling between the ligand and QD increases. The new states generated by the electronic couplings should promote delocalization of excitonic carriers to ligands and red-shift of the QD absorption.

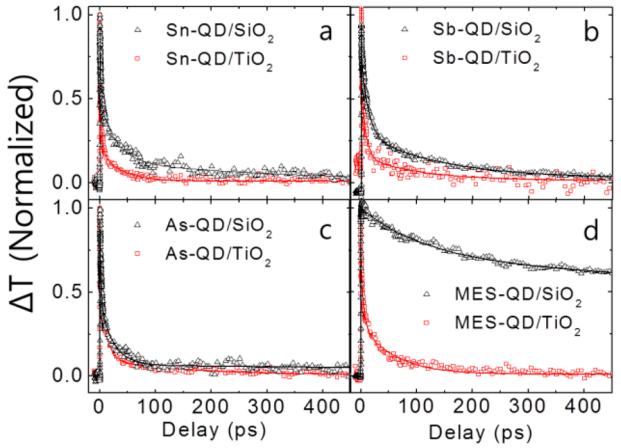

Figure 2. Transient absorption kinetic traces between QDs anchored to electron nonaccepting (SiO_2, black traces) and electron accepting (TiO_2, red traces) metal oxide substrates for (a) Sn-QD, (b) Sb-QD, (c) As-QD and (d) MES-QD.

Table 1. Triexponential Fitting Parameters and Amplitude Weighted Average Lifetimes of the Ultrafast Transient Absorption Measurements for QDs Capped with Different ICLs and for MES-QD on SiO_2 or on TiO_2

sample	A_1	τ_1 (ps)	A_2	τ_2 (ps)	A_3	τ_3 (ps)	τ_{ave} (ps)
Sn-QD/SiO_2	0.49	1.56	0.37	29	0.14	350	60
Sn-QD/TiO_2	0.52	0.38	0.38	3.1	0.15	37	6.6
Sb-QD/SiO_2	0.24	2.01	0.48	18.6	0.26	202	63
Sb-QD/TiO_2	0.47	0.80	0.34	7.0	0.11	100	15
As-QD/SiO_2	0.65	2.32	0.35	25.6	0.08	603	54
As-QD/TiO_2	0.51	0.98	0.40	11.4	0.09	150	19
MES-QD/SiO_2	0.34	116	0.10	712	0.69	5116	3200
MES-QD/TiO_2	0.39	0.45	0.35	4.8	0.26	61	18

To investigate QD bridging ligand effect on photogenerated electron dynamics, ultrafast transient absorption (TA) measurements were performed for QDs capped with the ICLs; QDs capped with 3-mercaptoethanesulfonate (MES) were used as controls (Figure 2), and extracted parameters were extracted using triexponential fittings (Table 1). The QDs were either adsorbed onto mesoporous TiO_2 films or placed on SiO_2 glass substrates. The samples were pumped by 95 fsec laser pulses at 400 nm, and white-light continuum probe pulses (420−820 nm) were used to measure the TAs (Figure S7). On the SiO_2 glass substrate, the three QD samples with ICLs recovered 29−53 times faster from photobleaching (60−110 ps) than did the control QDs with MES (3200 ps). Both the slow components

DOI: 10.1021/jacs.5b05787
J. Am. Chem. Soc. 2015, 137, 13827−13835

in the multiexponential fitting which usually correspond to radiative recombination, and the fast components that correspond more to nonradiative recombinations showed dramatically faster recoveries for the ICL-QD samples than for the control QD with MES. This difference suggests that the ICL assisted rapid removal of QD photoexcited carriers, presumably as a result of surface trap states induced by ICLs. On the TiO_2 substrate, the TA recovery of the control QDs capped with MES was much faster than on the SiO_2 substrate. On the TiO_2 substrate, MES-QDs can efficiently electron-transfer from QDs to the TiO_2, whereas Sn-QD, Sb-QD, and As-QD samples on TiO_2 substrates showed only slightly faster TA recovery than those on SiO_2. The electron transfer rate from QD to TiO_2 could be obtained as $k_{\text{electron transfer}} \cong k_{TiO_2/QDs} - k_{SiO_2/QDs} = 1/\tau_{ave(TiO_2/QDs)} - 1/\tau_{ave(SiO_2/QDs)}$, where $k_{TiO_2/QDs}$, $k_{SiO_2/QDs}$ are TA recovery rates of QD on TiO_2 and on SiO_2, respectively, and τ_{ave} is the average lifetime. The MES-QD showed the electron transfer rate of 5.6×10^{10} s^{-1}, which is comparable to the previously reported values. The electron transfer rate of QDs/TiO_2 with mercaptopropionic acids as the bridging ligand was reported to show $0.073-1.95 \times 10^{11}$ s^{-1}.[3] Sn-QD showed the fastest electron transfer rate of 1.4×10^{11} s^{-1}; this rate was 5.1×10^{10} s^{-1} for Sb-QD and 3.4×10^{10} s^{-1} for As-QDs. The rate constant of the control MES-QD was comparable to that of Sb-QD. ICL-QDs and MES-QDs have quite different surface ligands to each other that can greatly affect the charge transfers, and it is not straightforward to compare the rate constants. In contrast, the charge transfers of ICL-QDs/TiO_2 were dependent on the values of $\Delta\varepsilon$. Sn-QD has the smallest $\Delta\varepsilon$ and the fastest charge transfer rate, and as $\Delta\varepsilon$ of the ICLs of QDs increased their charge transfer to TiO_2 (Table 2) slowed. If $\Delta\varepsilon$ is hypothesized to represent the tunneling energy barrier height that dominantly determines the electron transfer, the transfer rate should be directly proportional to $\exp(-2(2m\Delta\varepsilon)^{1/2}R/\hbar)$,[26] where m is an electron mass, $\hbar$ is Plank constant, and R is the distance between TiO_2 and QD (0.278 nm for Sn-ICL, 0.265 nm for Sb-ICL, and 0.253 nm for As-ICL). The distance R was taken between two feet of perpendicular from the central atom in the two mutually perpendicular triangles each of which consists of the central atom and two adjacent bonding moieties (e.g., sulfur atoms). Values of $k_{\text{electron transfer}}/\exp(-2(2m\Delta\varepsilon)^{1/2}R/\hbar)$ for the Sn-, Sb-, and As-ICL QDs returned 5.16×10^{11} s^{-1}, 5.53×10^{11} s^{-1}, and 6.24×10^{11} s^{-1}, respectively. The three values are quite similar to each other, which suggests the strong $\Delta\varepsilon$ correlation for the three ICLs.

Table 2. Energy Gaps ($\Delta\varepsilon$) between the Conduction Band Edge of QD and the LUMOs of Sn-ICL, Sb-ICL, and As-ICL, the First Excitonic Absorption Peak Shift by Energy (meV) for Sn-QD, Sb-QD, and As-QD, and Electron Transfer Rates from QD to TiO_2 for Sn-QD, Sb-QD, and As-QD

sample	$\Delta\varepsilon$ (eV)	absorption energy shift (meV)	electron transfer rate from QD to TiO_2 (s^{-1})
Sn-QD	0.21	54	1.4×10^{11}
Sb-QD	0.77	19	5.1×10^{10}
As-QD	1.26	10	3.4×10^{10}

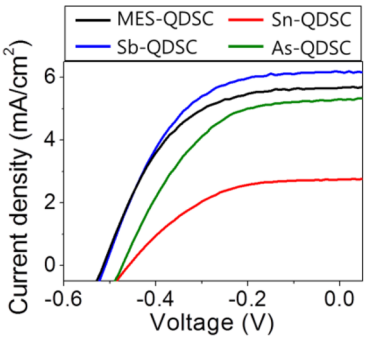

Figure 3. $J-V$ curves for the Sn-QDSC, Sb-QDSC, As-QDSC, and the control MES-QDSC.

Recently, Wang et al. reported that electron transfer occurs by nonresonant quantum tunneling in donor-bridge-acceptor systems, where the electronic coupling strength can be tuned by changing the molecular bridge length and chemical structures.[27] However, these molecular geometries are similar among our ICLs, so this tuning of the electronic coupling is not possible; therefore it seems to occur mostly as a result of the differing tunneling energy barrier heights.

To study the effect of QDs capped with different ICLs when the QDs are incorporated as the active component of sensitized solar cells, we fabricated QDSCs that include Sn-QDs, Sb-QDs, and As-QDs, and measured the photovoltaic properties of the QDSCs. ICL-QDs and MES-QDs were adsorbed onto mesoporous TiO_2 film. They were further fabricated for QDSCs with CuS counter electrode and 1 M polysulfide electrolyte. A series of post-treatment procedures were performed. For the QD adsorbed TiO_2 films, CdS deposition treatment was performed to form passivation layers.[28] The CdS layers may also function as interlayers to mitigate lattice mismatch for post-treatment ZnS layer deposition. The CdS deposition significantly improved the photovoltaic properties of the QDSCs (Figure S8, Table S4). We also tested whether CdS deposition before QD adsorption yielded cascading energy levels from CdSe QDs to TiO_2,[29] but the CdS deposition degraded photovoltaic efficiency, possibly due to the ill-defined interfaces created by CdS deposition (Figure S8, Table S4). Thermal annealing and ZnS overcoating process followed the CdS deposition to reduce the back electron transfers.[14,30] $J-V$ curves (Figure 3) were obtained from the QDSCs fabricated from the three ICLs. The QDSC fabricated from Sb-QDs (noted as Sb-QDSC) showed the highest short circuit current density among the three QDSCs (Sb-QDSC, Sn-QDSC, and As-QDSC) (Table 3). PCE of Sb-QDSC was 1.67%, which was followed by 1.24% for As-QDSC and 0.61% Sn-QDSC (Table 3). The control QDSC fabricated using MES-QD showed the short circuit current density of 5.66 mA/cm^2 and the PCE of

Table 3. Open-Circuit Voltages, Short-Circuit Current Densities, Fill Factors, and Power Conversion Efficiencies for the Sn-QDSC, Sb-QDSC, As-QDSC, and the Control MES-QDSC

	V_{oc} (V)	J_{sc} (mA/cm^2)	FF (%)	PCE (%)
MES-QD	0.51	5.66	54	1.56
Sn-QD	0.46	2.74	48	0.61
Sb-QD	0.51	6.17	53	1.67
As-QD	0.47	5.30	50	1.24

DOI: 10.1021/jacs.5b05787
J. Am. Chem. Soc. 2015, 137, 13827−13835

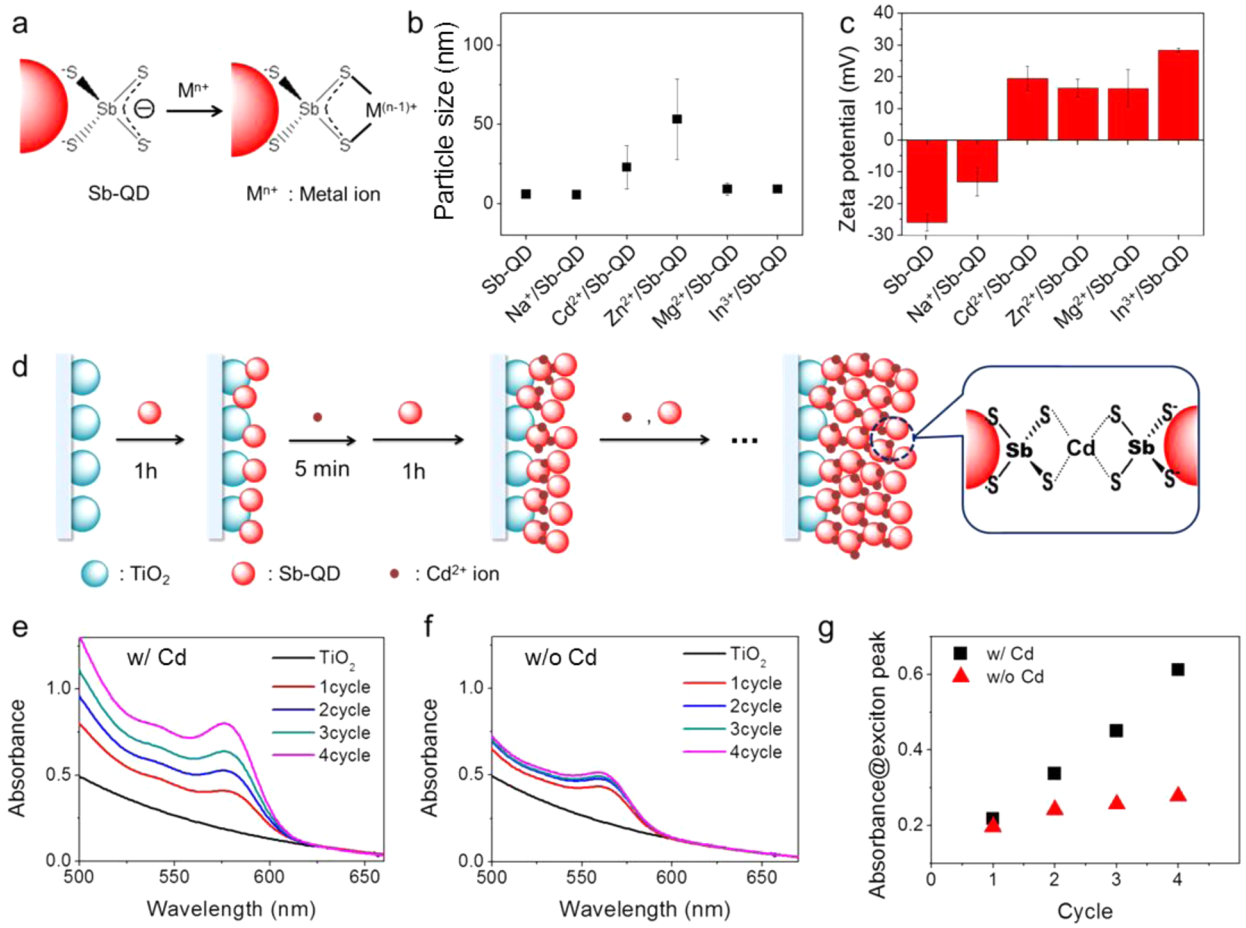

Figure 4. (a) Scheme of metal−ligand coordination between Sb-QD and metal ions. particle size distribution (b) and zeta potential (c) of Sb-QDs in solution and upon the additions of excess Na^+, Cd^{2+}, Zn^{2+}, Mg^{2+}, or In^{3+} ions. (d) Scheme of all-inorganic layer-by-layer Sb-QD assembly through coordinations by Cd^{2+} ions. (e) Absorption spectra of TiO_2 film before and after the layer-by-layer Sb-QD assembly cycles of one to four. (f) Absorption spectra of TiO_2 film before and after the control Sb-QD assembly cycles without the coordinating by Cd^{2+} ions. (g) Absorbance values at the first Sb-QD excitonic peak for the layer-by-layer Sb-QD assemblies (black squares) and for the control Sb-QD assemblies (red triangles).

1.56%. Only Sb-QDSC showed better J_{sc} and PCE than the control QDSC (MES-QD). The order of decrease in J_{sc} and PCE (Sb-QDSC > As-QDSC > Sn-QDSC) differed from the order of decrease of electron transfer rate (Sn-QD > Sb-QD > As-QD) determined by the TA measurements. Sn-QD had the fastest electron transfer rate, but the Sn-QDSC showed the poorest J_{sc} and PCE.

We hypothesize that the notably lower energy position of the Sn-ICL HOMO when compared with Sb-QD and As-QD HOMOs may have hindered hole transfer from QDs. Sb-QD showed faster electron transfer rate than As-QD, and Sb-QDSC exhibited both higher J_{sc} and PCE than in As-QDSC. In all three ICL-QDs, the electron transfer rate to TiO_2 was heavily dependent on the energy gap related to the QD conduction level, whereas the J_{sc} and PCE showed dependence on the gaps related to the QD conduction and valence levels.

In incident-photon-to-current efficiency (IPCE) studies, Sb-QDSC showed light harvesting at longer wavelengths than did MES-QDSC (Figure S9); this difference accords well with the absorption spectra (Figure 1b).

QDSCs based on LbL-assembled QD multilayers can offer a unique opportunity to tune the layers to selectively catch photons and thus to flexibly tune the light harvesting characteristics. Sequential spin-casting, chemical bath deposition, and electrophoretic deposition have been used to assemble QD multilayers, but these processes allow only limited control over the nanostructures.[31−33] Ordered arrays or films of nanoparticles have been assembled using dithiol linkers,[34] DNA hybridization,[35] and substrate-receptor binding.[36] We have studied electrostatic LbL assemblies of QD multilayers for QDSCs, which allowed very sophisticated control over the layer nanostructures.[14] Murray and co-workers reported the monolayer or multilayer gold nanoparticle films networked using multiple carboxylate-metal ion-carboxylate bridges.[37] Herein, we have further extended the LbL process of assembling QD multilayers for PV devices by exploiting metal−ligand coordination interactions between ICLs and metal cations. ICL-QDs can be a building block for all-inorganic LbL assembled QD multilayers in which metal ions mediating the metal−ligand coordination bonds. The outward terminal sites of ICLs can have a strong affinity to metal ions and may form a bridging coordination bond between ICLs from different QDs. Sb-ICLs on QDs expose the dithiocarboxyl group which can sandwich a metal ion to form a four-membered chelate ring.[38] Because Sb-QDSC showed the highest J_{sc} and PCE, we made it a model system to study the multilayer QDSCs. To investigate coordination bonds between ICLs and metal ions, excess amounts (10^5 molar equivalents

DOI: 10.1021/jacs.5b05787
J. Am. Chem. Soc. 2015, 137, 13827−13835

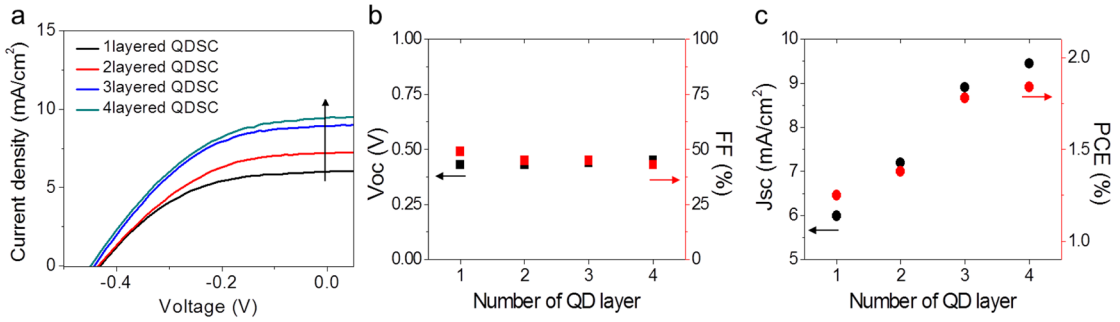

Figure 5. (a) $J-V$ curves of all-inorganic QDSCs that contain Sb-QD layers of one to four by layer-by-layer assemblies using Cd ion coordinations. Plots of photovoltaic properties of the four devices: (b) Open-circuit voltages (black squares) and fill factors (red square), (c) short-circuit current densities (black circles) and power conversion efficiencies (red circles).

per QD) of Na^+, Cd^{2+}, Zn^{2+}, Mg^{2+}, or In^{3+} ions were introduced to Sb-QDs in formamide solution (Figure 4a). Upon metal cation binding, particle size distribution and zeta potentials were measured (Figure 4b,c). Sb-QDs treated with Zn^{2+} had particle size ~50 nm, which indicates slight aggregation. Cd^{2+} treated Sb-QDs also showed some aggregations showing the particle size of ~20 nm. All Sb-QDs treated with other ions had particle sizes similar to untreated Sb-QDs. In the case of Cd^{2+}, Zn^{2+}, Mg^{2+} and In^{3+} treated Sb-QDs, the zeta potential changed negative to positive, whereas Sb-QDs treated with Na^+ showed negative zeta potential but with a significantly reduced magnitude than that of initial Sb-QDs; this difference indicates that Na^+ binds weakly to Sb-ICL. The aggregation and reversal of zeta potential in the presence of Zn^{2+} or Cd^{2+} suggest that these cations can strongly bind onto Sb-ICLs and at the same time form efficient bridges between neighboring Sb-ICLs. This capability is well suited to our LbL method of fabricating ICL-QDs by exploiting mediating coordination cations. We selected Cd^{2+} as the bridging cation between the Sb-QD layers because Zn^{2+} might alter the surfaces of CdSe QDs by forming ZnSe shells on them. Multilayers of Sb-QDs were prepared on mesoporous TiO_2 films using the Cd ion bridging coordinations. To study dependence on the number of QD layers, identical Sb-QDs were used for the multilayers. Two solutions were prepared: Sb-QD aqueous solution (pH 10) with 100 mM NaCl salt and Cd ion solution which contains dissolved $Cd(NO_3)_2$ in ammonia–water.

The mesoporous TiO_2 film substrate was dipped alternately into the Sb-QD solution for 1 h and the Cd ion solution for 5 min, with washing in water for 30 s between dippings (Figure 4d). As a control the LbL assembly experiment was repeated without the Cd-ion dipping process. The number of dipping cycles corresponded well with the LbL assembled QD layers. The absorbance from QDs increased linearly with the number of cycles (Figure 4e), whereas the control devices the QD absorbance increased slowly and in a saturating fashion as the number of dipping cycles increased (Figure 4f). Four cycles of dipping increased the absorbance values at the first excitonic QD peak by 280% in the assemblies with coordinating metal ions, but by only 40% in the assemblies without them (Figure 4g). All-inorganic QDSCs were fabricated using Cd ion coordination-assisted LbL assembled Sb-QD multilayers as the active component. The PV device fabrication was identical to that of single-layer Sb-QDSCs other than the active multilayers. Devices with one to four Sb-QD layers were fabricated to study how the number of layers affects J_{sc} and PCE. As the number of QD layers increased from one to four, J_{sc} increased from 5.99 to 7.20, 8.91, and 9.45 mA/cm^2 (Figure 5a), due to the increase in light-harvesting efficiency with the increase in the number of layers. Open-circuit voltages and fill factors did not show much dependence on the number of QD layers (Figure 5b). As a result, PCE increased from 1.25% to 1.84% as the number of layers increased from one to four (Figure 5c). These results demonstrate that extra light absorbed by the additional QD layers can be successfully transported to the anode through the QD layers.

CONCLUSIONS

We have synthesized three different ICLs for QDs: SnS_4^{4-}, SbS_4^{3-} and AsS_3^{3-}. When ligand-exchanged by the three ICLs, QDs showed the absorption shifts due to interactions between the conduction band of QD and the LUMO of ICL. QDs capped with Sn-ICLs showed the largest red shift. UPS and optical studies revealed that Sn-ICL had the smallest energy gap between the LUMO and the QD conduction band edge, which suggests strong electronic couplings between the two states. The energy gap has also heavily influenced the rates of electron transfer to the TiO_2 matrix; this rate was fastest for Sn-QD (1.4×10^{11} s^{-1}) which was 2.5 times faster than the control MES-QD. Because the three ICLs are thought to share similar molecular geometries, the energy gaps may have dominantly influenced the tunneling barrier height that determines the electron transfer rates. We have fabricated QDSCs using the three ICL-QDs and measured the PV properties. Sb-QDSC showed the largest J_{sc} and highest PCE, possibly due to the combination of electron and hole dynamics. Sn-QDs may have the strongest electron coupling with QDs, but the HOMO level gap of Sn-ICL to the QD valence level was largest among the three ICLs; this high level may have formed a barrier when incorporated into the PV device. In the case of organic capping ligands, it is typically the size of ligand (e.g., alkyl chain length) that critically governs the carrier dynamics and thus greatly affects the photovoltaic properties when incorporated in the solar cells. In contrast, the HOMO LUMO energy levels with respect to the QD bands become very important for ICL-QDs. Because ICLs can be exempt from the high energy barrier which is quite inherent for organic ligands, a very efficient QDSC that exceeds the performance attainable by organic capped QDs can be promised when the energy levels of ICLs are properly controlled. We have also exploited the metal ion coordination bonds between ICLs to LbL-assembled multilayers of ICL-QDs bridged by Cd ions. All-inorganic multilayer QDSCs were fabricated using Sb-QDs and Cd ions, and the PV properties were investigated for the dependence on the number

DOI: 10.1021/jacs.5b05787
J. Am. Chem. Soc. 2015, 137, 13827–13835

of QD layers. The QDSC with four layers of Sb-QDs showed 150% increase in PCE compared with that of single-layered QDSC.

EXPERIMENTAL SECTION

Materials. Cadmium acetylacetonate (99.9%), oleic acid, tech. (90%), selenium pellets, (<4 mm, 99.99%), sodium sulfide, Trioctylphosphine (90%), 1-octadecene, tech. (90%), oleylamine, tech. (70%), 3-mercaptoethanesulfonate, sodium sulfide, pyridine (99.0%), zinc acetate (99.99%), cadmium nitrate tetrahydrate, zinc nitrate hydrate hydrate (99.999%), magnesium nitrate hexahydrate (99%), indium nitrate hydrate were purchased from Aldrich. Arsenic(III) sulfide (99.9%) was purchased from Alfa Aesar, Sodium thioantimonate(V) nonahydrate was purchased from MERCK.

Synthesis of Metal Chalcogenide Complexes. Na_4SnS_4 was prepared as described previously.[8,16] Briefly, 183 mg of SnS_2 was reacted with 2 equiv moles of Na_2S in 10 mL of D.I. solution at pH = 11−12. The resultant $Na_4SnS_4{\cdot}xH_2O$ was precipitated by adding acetone, then centrifuged and dried. Most of crystalline water can be removed by moderate heating at 100−200 °C. Na_3AsS_3 was also prepared according as described previously.[8] Briefly, 492 mg of As_2S_3 powder and 3 equiv moles of Na_2S were mixed in 20 mL of D.I. overnight. The resultant Na_3AsS_3 aqueous solution was precipitated by adding acetone, then centrifuged and dried. Na_3SbS_4 was prepared by dissolving 481.1 mg of $Na_3SbS_4{\cdot}9H_2O$ crystalline powder with excess Na_2S in 20 mL of D.I. solution. The mixed aqueous solution refluxed overnight to achieve a transparent solution. Without excess Na_2S, the solution easily turns to brown precipitation after cooling. Na_3SbS_4 aqueous solution was precipitated by adding acetone, then centrifuged and dried. It was washed with ethanol.

Synthesis of CdSe Quantum Dots. CdSe quantum dots were synthesized using slightly modified procedures previously described.[39] As a Cd precursor, 0.6 mmol of cadmium acetylacetonate hydrate was dissolved in 1.8 mmol of oleic acid at 100 °C under vacuum. The solution was cooled to room temperature (RT), then mixed with Se precursor, which had been prepared by dissolving 3.0 mmol of Se shots in 3.0 mL of trioctylphosphine in glovebox. Then 24.0 mL of octadecene and 2.0 mL of oleylamine were loaded into a 50 mL threeneck flask and heated to 310 °C under N_2 gas flow. At this temperature, the mixture of Cd and Se precursors was quickly injected into the reaction flask, and the temperature was maintained at 280 °C. The reaction mixture was kept stirred until CdSe nanocrystals had reached the desired size. Then the mixture was cooled to RT and diluted using hexanes. For purification, the product mixture was precipitated by adding excess methanol, collected by centrifugation, and redispersed in a small amount of chloroform.

Surface Modification of Quantum Dots. CdSe QDs were ligand exchanged by ICLs and 3-mercaptoethanesulfonate (MES) as organic capping ligands. For ICLs modification, we used one phase exchange process. As-synthesized QDs were pyridine-exchanged. Purified QDs were mixed with excess pyridine and refluxed overnight. Pyridine-exchanged QDs were precipitated using hexane, then centrifuged and dried. Aqueous solutions with excess ICL were poured into the QD precipitates, and the mixtures were stirred until they became clear. ICL-QDs were purified by dialysis using an Amicon 50-kDa cutoff centrifugal filter and precipitation with acetonitrile. QDs surface-modified with MES were obtained using a two-phase exchange process. Excess (typically $>10^6$ time the number of QDs) of MES was dissolved in 100 mM of sodium bicarbonate buffer solution. Purified QDs were added to the buffer solution and further stirred for ≥2 h at RT. The QDs were transferred from the organic layer to the buffer layer. To remove excess free surface ligands, the QD solution was dialyzed three times using an Amicon 50-kDa cutoff centrifugal filter.

Metal Ion Assisted Layer-by-Layer Assembly of All-Inorganic QD Multilayer. Before multilayer assembly, we investigated coordination bonding between ICLs modified QDs and metal ions. ICL-QDs were prepared in 100 μL of 1 μM formamide solution and metal ion solutions were prepared in 1 mL of 0.1 M metal nitrate formamide solution. For multilayer assembly of QDs, we used 0.1 M of Cd-ammonia complexes prepared by adding 0.26 mL of 29% ammonia solution to $Cd(NO_3)_2$ aqueous solution. The FTO/TiO_2 substrate was dipped into the ICL-QD solutions for >1 h at pH 10, then washed with water for 30 s. For multilayered QDs, the cycle of alternative dipping into the Sb-QD solution and Cd^{2+} ion solution was repeated for the desired number of cycles.

Device Fabrication. QDs were deposited onto mesoporous TiO_2 which is ∼5 μm. To obtain TiO_2/ICL QDs, the TiO_2 photoanode were dipped into QD solutions for a few hours. The ICL-QDs became linked directly to TiO_2 through ICLs. In TiO_2/MES-QD, the MES-QDs are negatively charged at their surfaces and are therefore adsorbed onto TiO_2 by electrostatic interaction. After the QD-deposited electrode was rinsed with an appropriate solvent, three steps were conducted for post-treatment. To achieve a CdS passivation layer, photoanodes with adsorbed QDs were dipped into 0.1 M $Cd(NO_3)_2$ MeOH solution and 0.1 M Na_2S aqueous solution alternatively for 30 s each, then annealed at 250 °C for 30 min. Then a ZnS passivation layer was deposited by dipping the photoanode into 0.1 M Zinc acetate in MeOH solution and 0.1 M Na_2S aqueous solution alternatively for 1 min each. After post-treatment, the photoanode was assembled facing a counter electrode into a cell. The counter electrode had been prepared by deposition of CuS nanoparticles onto FTO glass.[40] The cell was then sealed with a 50-μm-thick transparent hot-melt film (Himilan of Mitsui-DuPont polychemical) by hot-pressing. The electrolyte was injected into the interelectrode space from the counter electrode side through a predrilled hole, which was then sealed with a Himilan sheet and a thin glass slide cover by heating. The polysulfide electrolyte solution was prepared freshly before each measurement by dissolving 1.0 M Na_2S and 1.0 M S in water. A solar simulator (model 66902) from Newport, which has a 300-W xenon lamp with an irradiance of 100 mW cm^{-2} (equivalent to one sun at AM1.5G) at the surface of the solar cell, was used. The current−voltage (J−V) characteristics of the cell were obtained by applying an external bias potential to the cell and measuring the photocurrent using an electrochemical analyzer (IVIUM CompactStat). The incident photon-to-current conversion efficiency (IPCE) was measured using a photomodulation spectroscopy setup (Merlin, Oriel) with monochromatic light from a xenon lamp. The power density of the monochromatic light was calibrated using a Si photodiode certified by the U.S. National Institute for Standards and Technology (NIST).

Characterization. The absorption spectra of QD-deposited TiO_2 films were obtained using a UV−visible spectrophotometer (Agilent 8453). Ultraviolet photoelectron spectroscopy was conducted using an AXIS-NOVA instrument (Kratos, Inc.) and using He I (21.22 eV) photon lines from a discharge lamp under 3.0×10^{-9} Torr. The ICL films were deposited on a commercial ITO substrate by drop casting and drying ICL aqueous solutions. The thickness of the ICL films was thick enough to eliminate background signal from the ITO substrate. For femtosecond transient absorption spectroscopy, the laser sources were Coherent Libra regenerative amplifier (50 fs, 1 kHz, 800 nm) seeded by a Coherent Vitesse oscillator (50 fs, 80 MHz). Laser pulses (800 nm wavelength) were obtained from the regenerative amplifier's output, and 400 nm wavelength laser pulses were obtained using a BBO doubling crystal. The samples were pumped at 400 nm and probed with a white-light continuum. The probe pulses (420−820 nm) were generated by focusing a small portion (∼5 μJ) of the fundamental 800 nm laser pulses into a 2 mm-thick sapphire plate. A polarizer and a half waveplate were used to adjust the linear polarization of the pump pulse to be perpendicular to that of the probe pulse. The cross-polarization eliminates any early contribution from coherent artifacts. Pump-induced changes of transmission (ΔT/T) of the probe beam were monitored using a monochromator/PMT configuration with lock-in detection. The pump beam was chopped at 83 Hz and this was used as the reference frequency for the lock-in amplifier. All measurements were performed with the samples placed in an evacuated cryostat at RT.

Density Functional Theory Calculation. To understand the orbital characters of HOMO and LUMO levels of the Sn-ICL, Sb-ICL, and As-ICL molecules, we performed density functional theory (DFT)

DOI: 10.1021/jacs.5b05787
J. Am. Chem. Soc. 2015, 137, 13827−13835

calculations on the hybrid functionals[41] using the generalized gradient approximation (GGA) method implemented with the projector augmented wave (PAW)[41,42] pseudopotential by the Vienna ab initio Simulation Package (VASP).[43,44] We adopted (i) a 2 × 2 × 2 Monkhorst–Pack *k*-point mesh centered at **Γ**[45] for a 15 × 15 × 15 Å^3 supercell containing a molecule embedded with vacuum regions, (ii) a 500 eV plane-wave cutoff energy, and (iii) a H-passivation for all the ICL molecules to mimic the effect of charged state of the sulfur atoms. We explicitly treated the 5 valence electrons for As ($4s^24p^3$), 5 for Sb ($5s^25p^3$), 4 for Sn ($5s^25p^2$) and 6 for S ($3s^23p^4$). All structural relaxations were performed with a Gaussian broadening of 0.05 eV.[46] The ions were relaxed until the forces on them were less than 0.01 eV Å^{-1}. To obtain the band gap, we have computed the entire density of states for the three ICLs. Typically, DFT calculations tend to underestimate the band gaps. For better calculations, we have adopted the hybrid functional calculations of HSE06.[47,48]

■ ASSOCIATED CONTENT

Supporting Information

The Supporting Information is available free of charge on the ACS Publications website at DOI: 10.1021/jacs.5b05787.

EDX, NMR, mass spectra, UPS, Tauc plot, DFT calculation of ICLs, FTIR, size distribution, zeta potential, TA of ICL-QDs, UPS of QD, IPCE of MES-QDSC, and Sb-QDSC, post-treatments of QDSCs. (PDF)

■ AUTHOR INFORMATION

Corresponding Author

*sungjee@postech.ac.kr

Author Contributions

#H.J. and S.C. contributed equally.

Notes

The authors declare no competing financial interest.

■ ACKNOWLEDGMENTS

This research was supported by Basic Science Research Program through the National Research Foundation of Korea(NRF) funded by the Ministry of Education, Science and Technology NRF-2013R1A1A2005582. S. Choi acknowledges the support from Global Ph.D. Fellowship program by NRF. T. C. Sum acknowledges the financial support from the Nanyang Technological University start-up grant M4080514, SPMS collaborative Research Award M4080536; the Ministry of Education AcRF Tier 1 grant RG101/15 and Tier 2 grants MOE2013-T2-1-081 and MOE2014-T2-1-044; and from the Singapore National Research Foundation through the Singapore–Berkeley Research Initiative for Sustainable Energy (SinBeRISE) CREATE Program and the Competitive Research Program NRF2014NRF-CRP002-036.

■ REFERENCES

(1) Kamat, P. V. *J. Phys. Chem. C* **2008**, *112*, 18737–18753.
(2) Talapin, D. V.; Lee, J. S.; Kovalenko, M. V.; Shevchenko, E. V. *Chem. Rev.* **2010**, *110*, 389–458.
(3) Robel, I.; Subramanian, V.; Kuno, M.; Kamat, P. V. *J. Am. Chem. Soc.* **2006**, *128*, 2385–2393.
(4) Dibbell, R. S.; Watson, D. F. *J. Phys. Chem. C* **2009**, *113*, 3139–3149.
(5) Dibbell, R. S.; Youker, D. G.; Watson, D. F. *J. Phys. Chem. C* **2009**, *113*, 18643–18651.
(6) Hyun, B. R.; Bartnik, A. C.; Sun, L. F.; Hanrath, T.; Wise, F. W. *Nano Lett.* **2011**, *11*, 2126–2132.
(7) Kovalenko, M. V.; Scheele, M.; Talapin, D. V. *Science* **2009**, *324*, 1417–1420.
(8) Kovalenko, M. V.; Bodnarchuk, M. I.; Zaumseil, J.; Lee, J. S.; Talapin, D. V. *J. Am. Chem. Soc.* **2010**, *132*, 10085–10092.
(9) Lee, J. S.; Kovalenko, M. V.; Huang, J.; Chung, D. S.; Talapin, D. V. *Nat. Nanotechnol.* **2011**, *6*, 348–352.
(10) Stolle, C. J.; Panthani, M. G.; Harvey, T. B.; Akhavan, V. A.; Korgel, B. A. *ACS Appl. Mater. Interfaces* **2012**, *4*, 2757–2761.
(11) Choi, S.; Jin, H.; Kim, S. *J. Phys. Chem. C* **2014**, *118*, 17019–17027.
(12) Choi, S.; Jin, H.; Bang, J.; Kim, S. *J. Phys. Chem. Lett.* **2012**, *3*, 3442–3447.
(13) Jin, H.; Choi, S.; Lee, H. J.; Kim, S. *J. Phys. Chem. Lett.* **2013**, *4*, 2461–2470.
(14) Jin, H.; Choi, S.; Velu, R.; Kim, S.; Lee, H. J. *Langmuir* **2012**, *28*, 5417–5426.
(15) Jin, H.; Choi, S.; Lim, S. H.; Rhee, S. W.; Lee, H. J.; Kim, S. *ChemPhysChem* **2014**, *15*, 69–75.
(16) Guyot-Sionnest, P.; Lhuillier, E.; Liu, H. *J. Chem. Phys.* **2012**, DOI: 10.1063/1.4758318.
(17) Frederick, M. T.; Amin, V. A.; Weiss, E. A. *J. Phys. Chem. Lett.* **2013**, *4*, 634–640.
(18) Schiwy, W.; Pohl, S.; Krebs, B. *Z. Anorg. Allg. Chem.* **1973**, *402*, 77–86.
(19) Mereiter, K.; Preisinger, A. *Acta Crystallogr., Sect. B: Struct. Crystallogr. Cryst. Chem.* **1979**, *B35*, 19–25.
(20) Palazzi, P. M. *Acta Crystallogr., Sect. B: Struct. Crystallogr. Cryst. Chem.* **1976**, *B32*, 3175–3177.
(21) Voznyy, O. *J. Phys. Chem. C* **2011**, *115*, 15927–15932.
(22) Hassinen, A.; Gomes, R.; Nolf, K. D.; Zhao, Q.; Vantomme, A.; Martins, J. C.; Hens, Z. *J. Phys. Chem. C* **2013**, *117*, 13936–13943.
(23) Dubois, F.; Mahler, B.; Dubertret, B.; Doris, E.; Mioskowski, C. *J. Am. Chem. Soc.* **2007**, *129*, 482–483.
(24) Protesescu, L.; Nachtegaal, M.; Voznyy, O.; Borovinskaya, O.; Rossini, A. J.; Emsley, L.; Coperet, C.; Gunther, D.; Sargent, E. H.; Kovalenko, M. V. *J. Am. Chem. Soc.* **2015**, *137*, 1862–1874.
(25) Tvrdy, K.; Frantsuzov, P. A.; Kamat, P. V. *Proc. Natl. Acad. Sci. U. S. A.* **2011**, *108*, 29–34.
(26) Albinsson, B.; Eng, M. P.; Pettersson, K.; Winters, M. U. *Phys. Chem. Chem. Phys.* **2007**, *9*, 5847–5864.
(27) Wang, H.; McNellis, E. R.; Kinge, S.; Bonn, M.; Canovas, E. *Nano Lett.* **2013**, *13*, 5311–5315.
(28) Mu, L.; Liu, C.; Jia, J.; Zhou, X.; Lin, Y. *J. Mater. Chem. A* **2013**, *1*, 8353–8357.
(29) Lee, Y.-L.; Lo, Y.-S. *Adv. Funct. Mater.* **2009**, *19*, 604–609.
(30) Shen, Q.; Kobayashi, J.; Diguna, L. J.; Toyoda, T. *J. Appl. Phys.* **2008**, *103*, 084304.
(31) Luther, J. M.; Law, M.; Beard, M. C.; Song, Q.; Reese, M. O.; Ellingson, R. J.; Nozik, A. J. *Nano Lett.* **2008**, *8*, 3488–3492.
(32) Lee, H. J.; Bang, J.; Park, J.; Kim, S.; Park, S. M. *Chem. Mater.* **2010**, *22*, 5636–5643.
(33) Santra, P. K.; Kamat, P. V. *J. Am. Chem. Soc.* **2013**, *135*, 877–885.
(34) Rauf, S.; Glidle, A.; Cooper, J. M. *Langmuir* **2010**, *26*, 16934–16940.
(35) Alivisatos, A. P. *Science* **1996**, *271*, 933–937.
(36) Liu, J.; Mendoza, S.; Roman, E.; Lynn, M. J.; Xu, R. L.; Kaifer, A. E. *J. Am. Chem. Soc.* **1999**, *121*, 4304–4305.
(37) Zamborini, F. P.; Hicks, J. F.; Murray, R. W. *J. Am. Chem. Soc.* **2000**, *122*, 4514–4515.
(38) Bonamico, M.; Dessy, G.; Fares, V.; Scaramuzza, L. *J. Chem. Soc., Dalton Trans.* **1972**, *1*, 2515–2517.
(39) Yu, W. W.; Peng, X. G. *Angew. Chem., Int. Ed.* **2002**, *41*, 2368–2371.
(40) Yang, Z.; Chen, C.-Y.; Liu, C.-W.; Li, C.-L.; Chang, H.-T. *Adv. Energy Mater.* **2011**, *1*, 259–264.
(41) Blöchl, P. E. *Phys. Rev. B: Condens. Matter Mater. Phys.* **1994**, *50*, 17953.

(42) Kresse, G.; Joubert, D. *Phys. Rev. B: Condens. Matter Mater. Phys.* **1999**, *59*, 1758.
(43) Kresse, G.; Hafner, J. *Phys. Rev. B: Condens. Matter Mater. Phys.* **1993**, *47*, 558.
(44) Kresse, G.; Furthmüller, J. *Phys. Rev. B: Condens. Matter Mater. Phys.* **1996**, *54*, 11169.
(45) Monkhorst, H. J.; Pack, J. D. *Phys. Rev. B* **1976**, *13*, 5188.
(46) Elsässer, C.; Fähnle, M.; Chan, C. T.; Ho, K. M. *Phys. Rev. B: Condens. Matter Mater. Phys.* **1994**, *49*, 13975.
(47) Heyd, J.; Scuseria, G. E.; Ernzerhof, M. *J. Chem. Phys.* **2003**, *118*, 8207−8215.
(48) Heyd, J.; Scuseria, G. E.; Ernzerhof, M. *J. Chem. Phys.* **2006**, *124*, 219906.

DOI: 10.1021/jacs.5b05787
J. Am. Chem. Soc. 2015, 137, 13827−13835